PAPER

Check for updates

Mesoporous Co_3O_4 supported Pt catalysts for low-temperature oxidation of acetylene

Qi Wang, Jian Liu, [ID] * Yongheng Li, Zhen Zhao, [ID] Weiyu Song and Yuechang Wei

Three-dimensionally ordered mesoporous Co_3O_4 (meso-Co_3O_4) and its supported Pt catalysts were synthesized for the catalytic oxidation of acetylene. All the catalysts formed mesoporous structures and possessed high surface areas of 110–122 m^2 g^{-1}. Meso-Co_3O_4-supported Pt catalysts exhibited highly catalytic performances, and the 0.6Pt/meso-Co_3O_4 catalyst gave the lowest temperature of 120 °C for acetylene oxidation. It was concluded that the ordered mesoporous structure, with plenty of structural defects, good low-temperature reducibility and the high concentration of active oxygen species were responsible for the excellent catalytic performance of 0.6Pt/meso-Co_3O_4.

1. Introduction

Acetylene (C_2H_2) is mainly emitted from motor vehicle exhausts and petrochemical processing. It enhances the photochemical reaction and promotes the formation of secondary organic aerosols (SOAs) and ozone.[1–3] Catalytic oxidation is one of the most effective pathways to eliminate acetylene, in which the key issue is the development of the catalytic materials. However, as far as we know, there are few reports about catalysts for the catalytic oxidation of acetylene. Thus, it is very significant to explore a high performance catalyst for removing acetylene.

Co_3O_4 shows excellent catalytic performance and is widely used in many reactions, for example, CO oxidation,[4] ethylene oxidation,[5] formaldehyde oxidation (with[6] or without[7] noble metal promoters) and the oxidation of other organic molecules.[8] It is commonly accepted that the activity of the catalyst is closely related to its morphology and structure. Different structures and morphologies of Co_3O_4 have been reported, including nano-rod, nano-tube, nano-sheet, nano-sphere and multi-porous structures.[9,10] Three-dimensional ordered mesoporous metal oxides possess high surface area, large pore volume and controllable pore diameter, which have attracted more and more attentions for their special physicochemical properties. Bai *et al.*[11] prepared nano-Co_3O_4, 2D-Co_3O_4, and 3D-Co_3O_4 catalysts for the catalytic oxidation of formaldehyde. The result showed that 3D-Co_3O_4 catalyst exhibited the best catalytic performance for formaldehyde oxidation.

Pt particles supported on metal oxides were effective catalysts in the oxidation reaction.[12] Zhang *et al.*[13] reported that Pt/TiO_2 was the most active catalyst for HCHO oxidation when 1 wt% noble metal (Pt, Rh, Pd and Au) was supported on TiO_2. Compared with

metal oxide catalysts, oxide-supported Pt catalysts showed higher catalytic activity for the oxidation reaction. Tang *et al.*[14] prepared Pt/MnO_x–CeO_2 catalysts for the oxidation of formaldehyde. The presence of Pt active sites promoted the adsorption of formaldehyde and the effective activation of oxygen molecule.

Herein, we report the synthesis of meso-Co_3O_4 and meso-Co_3O_4-supported Pt catalysts for the oxidation of acetylene. The effects of mesoporous structure, lattice defect, oxygen species and low-temperature reducibility are investigated in terms of acetylene removal.

2. Experimental

2.1. Catalyst preparation

KIT-6 was synthesized according to the strategy reported previously.[15] Meso-Co_3O_4 was prepared using KIT-6 as the hard template. In a typical synthesis process of meso-Co_3O_4, 1.0 g of KIT-6 was added to a solution of $Co(NO_3)_2 \cdot 6H_2O$ in ethanol. The samples were evaporated to dryness at 60 °C. The products were calcined at 550 °C for 6 h. The hard template of KIT-6 was removed by NaOH solution (2 mol L^{-1}) at 60 °C. Orderedly meso-Co_3O_4 was obtained after centrifugation, washing with deionized water and drying at 100 °C. For comparison, the bulk-Co_3O_4 was prepared *via* the thermal decomposition of $Co(NO_3)_2 \cdot 6H_2O$ at 550 °C for 6 h.

The meso-Co_3O_4 and bulk-Co_3O_4 supported Pt catalysts were prepared by the means of $NaBH_4$ reduction. In a typical synthesis process, $HPtCl_4$ aqueous solution was mixed with PVP at 35 °C. Then 1 g of meso-Co_3O_4 or bulk-Co_3O_4 was added to the solution. The mixed solution was stirred for 4 h. Subsequently, $NaBH_4$ was added under rapidly stirring. The solid was centrifugal separation, washed with deionized water, dried at 100 °C for 8 h and calcined at 350 °C for 4 h. The final catalysts are marked as xPt/meso-Co_3O_4 or xPt/bulk-Co_3O_4 (x denotes the weight percentage of Pt element to the related catalyst, $x = 0.3$,

State Key Laboratory of Heavy Oil Processing, Beijing Key Lab of Oil & Gas Pollution Control, China University of Petroleum, 18# Fuxue Road, Chang Ping District, Beijing 102249, P. R. China. E-mail: liujian@cup.edu.cn

0.6 and 1.0). The content of Pt were measured by inductively coupled plasma atomic emission spectroscopy (ICP-AES).

2.2. Catalyst characterization

X-ray diffraction (XRD) patterns were tested by a powder meter (Bruker D8 Advance) using Cu Kα radiation ($\lambda = 0.154056$ nm), operating at 40 kV and 10 mA. Data were recorded in a 2θ of the low-angle from 0.5 to 3° and wide-angle range of 10–80°. N_2 adsorption–desorption isotherms and pore size distributions of the catalysts were tested on an automated gas sorption analyzer (Micrometrics TriStar II 3020). The samples were degassed for 4 h at 300 °C. Transmission electron microscopy (TEM) images were observed using a JEOL JEM 2100 instrument at an accelerating voltage of 200 kV. The catalysts were dispersed in ethanol, and dropped on a copper grid. Scanning electron microscopy (SEM) images measurements were obtained on a SU8010 instruments with the working voltages of 5 kV. Raman spectra were recorded on a Renishaw Laser Raman spectrometer with a laser excitation wavelength of 532 nm under room temperature. The spectra were obtained with resolution of 1 cm^{-1} and scanned from 100 to 1000 cm^{-1}. X-ray photoelectron spectra (XPS) were recorded on an AxiosmAX spectrometer with an Al Kα X-ray source. The charge-shifted spectra were calibrated using the C 1s photoelectron signal at 284.6 eV. The data were processed by XPS-PEAK software. O_2-TPD experiments were tested on a DAS-7000 instrument. 0.05 g of samples were pretreated in the O_2 flow (30 mL min^{-1}) at 300 °C for 1 h. The samples were cooled, then the carrier gas changed to pure He. The sample was heated by a flow (30 mL min^{-1}) of pure He from 30 °C to 850 °C at a rate of 10 °C min^{-1}. H_2-TPR experiments were also tested on the above instrument. 0.05 g of samples were pretreated in the N_2 flow at 300 °C for 1 h. The samples were cooled and reduced by a flow (30 mL min^{-1}) of a 10% H_2/90% N_2 mixture from 100 to 600 °C with a heating rate of 10 °C min^{-1}. The H_2 consumptions of the reduction band were calibrated by a standard CuO (99.998%) powder.

2.3. Catalytic activity test

The catalytic activities of the catalysts were tested in the fixed bed reactor. The samples (100 mg, 40–60 mesh) were placed in the middle of the reaction tube. The concentration of gases was detected by a SP-1000 chromatographic analyzer with a TCD detector. The reaction gas consisted of 50 ppm C_2H_2, 13 v% O_2 and balance gas N_2, and the total flow rate of the reactant was 60 mL min^{-1} (under standard condition). The gas hourly space velocity (GHSV) of the catalytic oxidation was 30 000 h^{-1}. The conversion rate of C_2H_2 was calculated by the following formula:

$$C_2H_2 \text{ conversion} = \frac{[C_2H_2]_{inlet} - [C_2H_2]_{outlet}}{[C_2H_2]_{inlet}} \times 100\%$$

3. Results and discussion

3.1. Structural and textural analyses

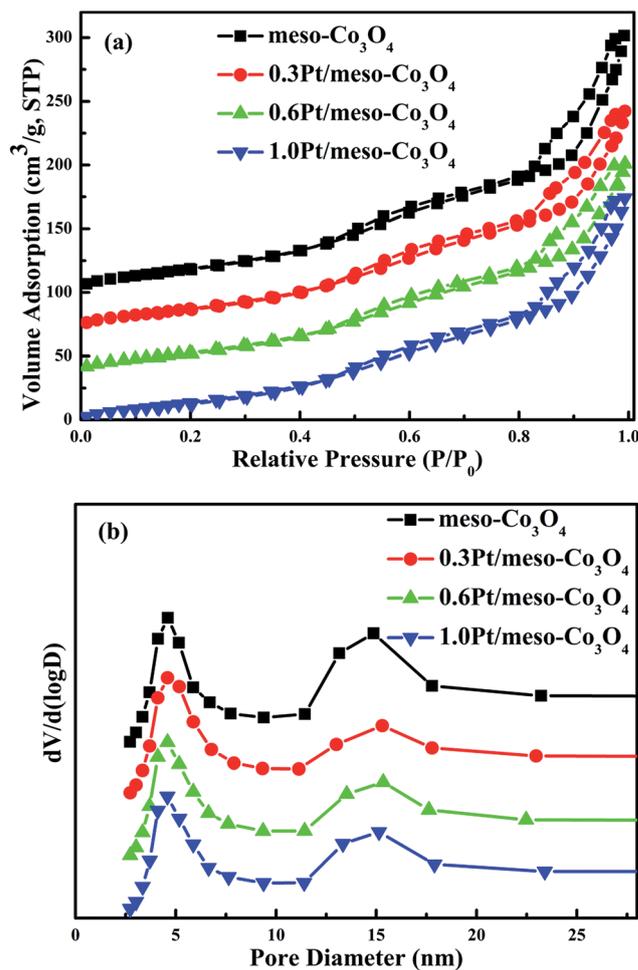N_2 adsorption–desorption isotherms and pore size distributions of the meso-Co_3O_4 and xPt/meso-Co_3O_4 are shown in

Fig. 1 (a) N_2 adsorption–desorption and (b) pore size distributions of meso-Co_3O_4, 0.3Pt/meso-Co_3O_4, 0.6Pt/meso-Co_3O_4 and 1.0Pt/meso-Co_3O_4.

Fig. 1a and b, respectively. All samples show type IV isotherms[16] with a H1 hysteresis loop, suggesting the presence of uniform mesopores. It is consistent with the low-angle XRD results (Fig. 2B). BET surface areas, average pore diameters and pore volumes of all samples are displayed in Table 1. All catalysts possess the average pore size of maximum distribution at 5 nm. The broad peak of pore size distribution at 15 nm can be attributed to interspace of the catalysts. The pore diameters, surface areas and pore volumes of xPt/meso-Co_3O_4 do not significantly reduce. The surface areas of meso-Co_3O_4 and xPt/meso-Co_3O_4 (110–122 m^2 g^{-1}) are much larger than those of bulk-Co_3O_4 and 0.6Pt/bulk-Co_3O_4 (8.1–8.4 m^2 g^{-1}). It indicates that most of Pt nanoparticles are dispersed on the surface of the catalysts.

From the wide-angle XRD patterns in Fig. 2A, all the catalysts show diffraction peaks at 19°, 31.3°, 36.9°, 38.2°, 44.5°, 55.6°, 59.4° and 65.3° (2θ), conforming the (111), (220), (311), (222), (400), (422), (511) and (440) planes.[17] It is consistent with the standard cobalt oxide spinel structure (JCPDS PDF# 43-1003). The loading of Pt particles rarely affects Co_3O_4 crystal. Fig. 2B shows the low-angle XRD patterns of the samples. The meso-Co_3O_4 and
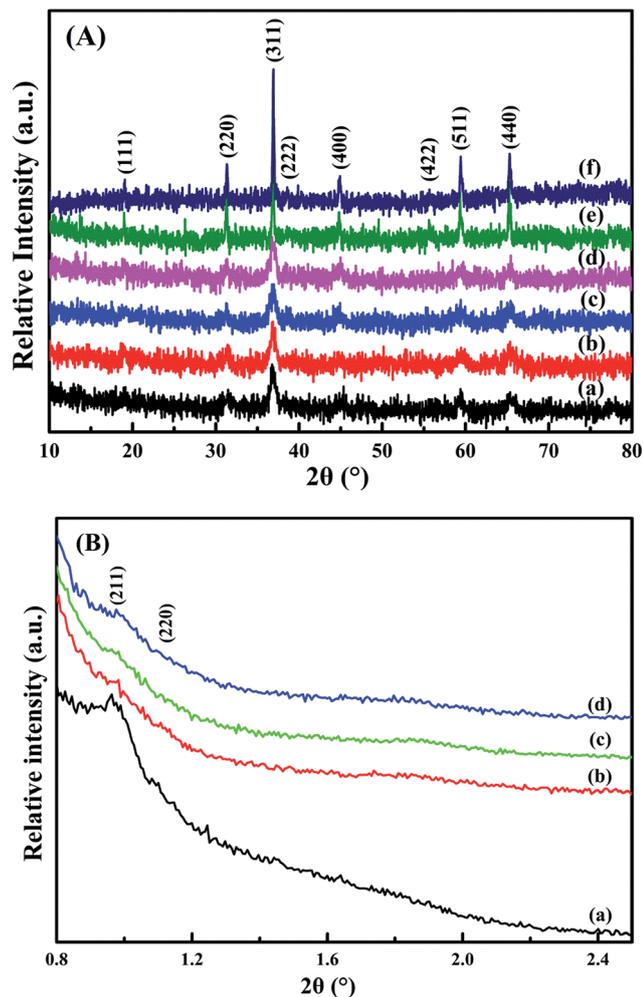
Fig. 2 (A) Wide-angle and (B) low-angle XRD patterns of (a) meso-Co_3O_4, (b) 0.3Pt/meso-Co_3O_4, (c) 0.6Pt/meso-Co_3O_4, (d) 1.0Pt/meso-Co_3O_4, (e) bulk-Co_3O_4 and (f) 0.6Pt/bulk-Co_3O_4.

Table 1 Textural properties of samples

Sample	Surface area ($m^2\ g^{-1}$)	Average pore diameter (nm)	Pore volume ($cm^3\ g^{-1}$)
Meso-Co_3O_4	122.0	8.4	0.38
0.3Pt/meso-Co_3O_4	111.5	7.9	0.33
0.6Pt/meso-Co_3O_4	110.9	7.8	0.32
1.0Pt/meso-Co_3O_4	110.0	8.2	0.33
Bulk-Co_3O_4	8.4	—	—
0.6Pt/bulk-Co_3O_4	8.1	—	—

xPt/meso-CO_3O_4 catalysts exhibit (211) and (220) diffraction peaks at 2θ angle 1° and 1.14°.[5] It indicates that the catalysts possess a three-dimensional orderedly mesoporous structure. The regularity of the mesoporous structure decreases after Pt loading.

Fig. 3 presents TEM images of the meso-Co_3O_4 and xPt/meso-Co_3O_4. All samples display orderedly mesoporous structure. Pt particles are dispersed on the surface of meso-Co_3O_4. Dispersive Pt particles may provide more active sites for the catalytic oxidation of acetylene. The loading of Pt does not
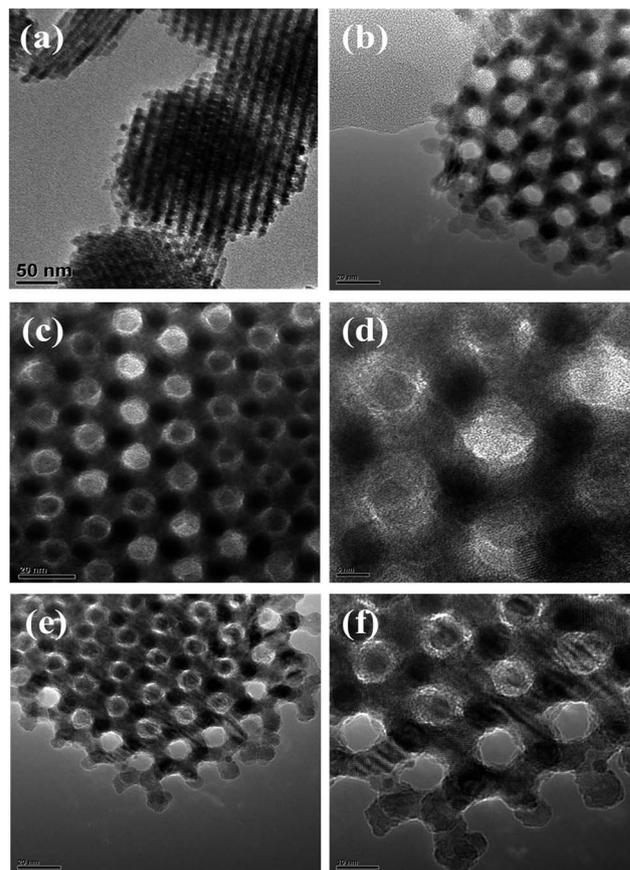

Fig. 3 TEM images of (a) meso-Co_3O_4, (b) 0.3Pt/meso-Co_3O_4, (c and d) 0.6Pt/meso-Co_3O_4 and (e and f) 1.0Pt/meso-Co_3O_4.

change the mesoporous structure. The orderedly mesoporous structure can facilitate the transport and diffusion of reactant and product molecules. Meanwhile, such a mesoporous structure can prevent Pt particles from leaching and aggregation because of the limitation of the special channels. By making a statistic analysis on the sizes of more than 200 Pt particles in the TEM images of the 1.0Pt/meso-Co_3O_4 sample, the particle size distribution of Pt particles are shown in Fig. 4. The mean diameter of Pt particles is about 2.9 nm.

Raman spectra of all the samples are shown in Fig. 5. Raman peaks at 195, 480, 518, 615 and 689 cm^{-1} correspond to the $F_{2g}^{(1)}$, E_g, $F_{2g}^{(2)}$, $F_{2g}^{(3)}$ and A_{1g} symmetries of crystalline Co_3O_4, respectively.[18] The peak at 689 cm^{-1} can be ascribed to Raman vibration of Co^{3+}–O^{2-}.[7] The overall enhancement of peak intensity in bulk-Co_3O_4 and 0.6Pt/bulk-Co_3O_4 samples should be due to the influence of crystallinity and the orientation effect during the Raman test. With the loading of Pt, Raman peak at 689 cm^{-1} shows an obvious shift to lower frequencies and the peak intensity decreases. The red shift indicates that xPt/meso-Co_3O_4 catalysts have a lattice defect or residual stress of the spinel structure.[19] The existence of lattice defect is beneficial for the formation of the oxygen vacancies.[20] The oxygen vacancies can activate, adsorb oxygen and provide the lattice sites of oxygen migration, resulting in the formation of highly active electrophilic oxygen species.[21] The decrease of the peak
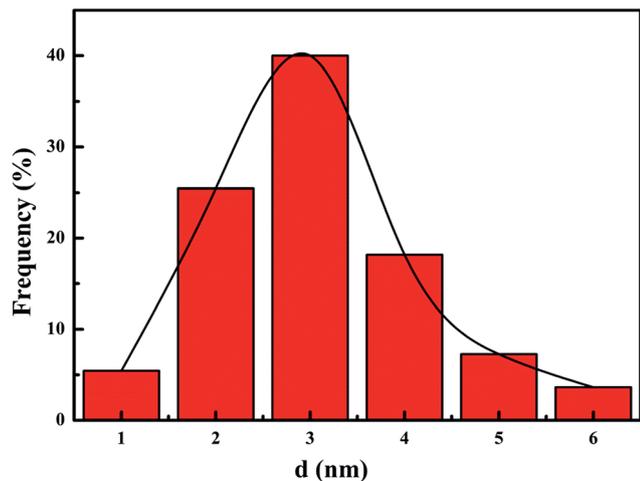
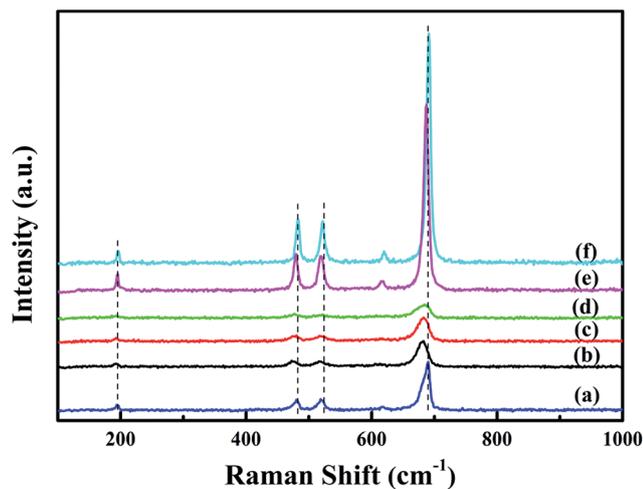Fig. 4 Pt particles size distribution of 1.0Pt/meso-Co$_3$O$_4$.

Fig. 5 Raman spectra of (a) meso-Co$_3$O$_4$, (b) 0.3Pt/meso-Co$_3$O$_4$, (c) 0.6Pt/meso-Co$_3$O$_4$, (d) 1.0Pt/meso-Co$_3$O$_4$, (e) 0.6Pt/bulk-Co$_3$O$_4$ and (f) bulk-Co$_3$O$_4$.

intensities is due to the decrease of Co^{3+}. It can be concluded that there is an electron transfer from Pt^0 to Co^{3+}.

3.2. The results of XPS

XPS is performed in order to gain the information of surface element compositions, chemical states and adsorbed oxygen species of catalysts. Pt 4f XPS spectra of xPt/meso-Co$_3$O$_4$ and 0.6Pt/bulk-Co$_3$O$_4$ are shown in Fig. 6A. The binding energies of 71.1, 74.2 and 77.3 eV can be assigned to Pt^0, Pt^{2+} and Pt^{4+} species, respectively.[22] This result indicates that both Pt^0 and Pt$^{\delta+}$ (Pt^{2+} and Pt^{4+}) species exist on the surface of Co$_3$O$_4$ support. Pt$^{\delta+}$ species is generally active species rather than metallic Pt in oxidation reaction.[23] Table 2 lists the relative amounts of Pt^0, Pt^{2+} and Pt^{4+} species on the surface of 0.6Pt/meso-Co$_3$O$_4$, 1.0Pt/meso-Co$_3$O$_4$ and 0.6Pt/bulk-Co$_3$O$_4$ by the means of XPS-peak-differentiation-imitating analysis. It is hard to calculate the content of the Pt species for 0.3Pt/meso-Co$_3$O$_4$. The Pt$^{\delta+}$
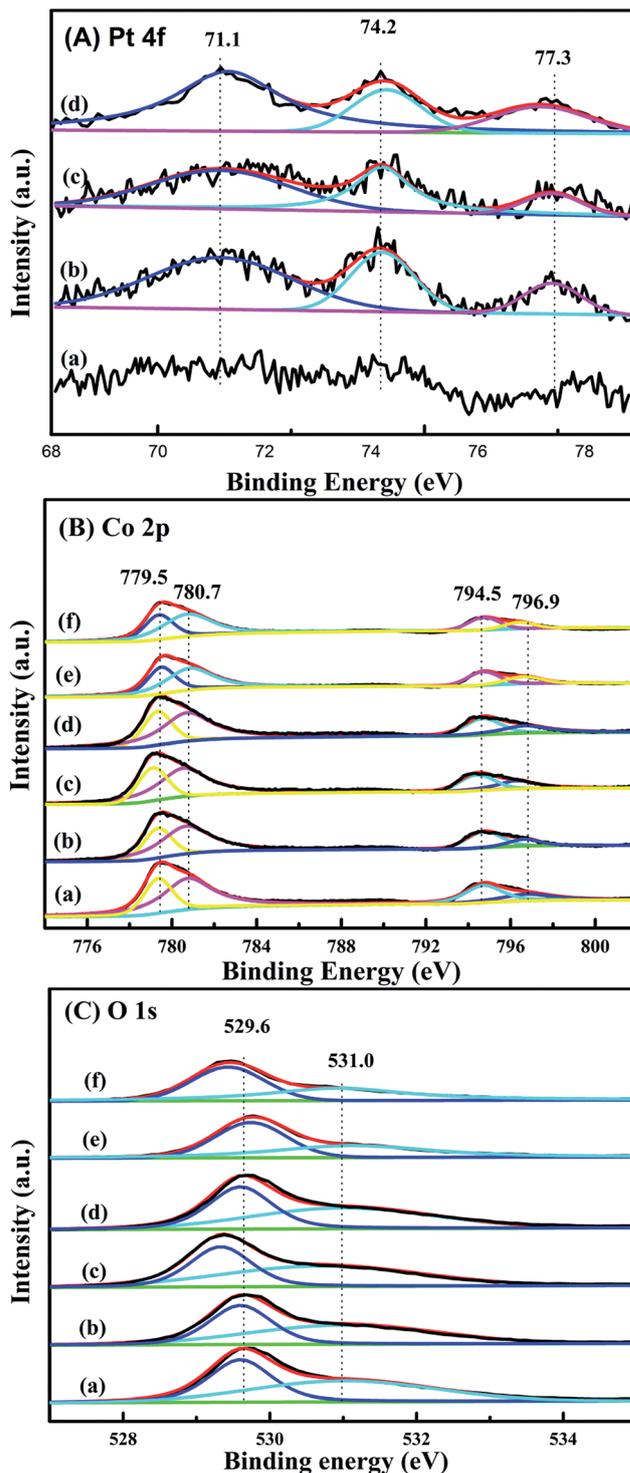

Fig. 6 (A) Pt 4f XPS spectra of (a) 0.3Pt/meso-Co$_3$O$_4$, (b) 0.6Pt/meso-Co$_3$O$_4$, (c) 1.0Pt/meso-Co$_3$O$_4$ and 0.6Pt/bulk-Co$_3$O$_4$. (B) O 1s and (C) Co 2p XPS spectra of (a) meso-Co$_3$O$_4$, (b) 0.3Pt/meso-Co$_3$O$_4$, (c) 0.6Pt/meso-Co$_3$O$_4$, (d) 1.0Pt/meso-Co$_3$O$_4$, (e) bulk-Co$_3$O$_4$ and (f) 0.6Pt/bulk-Co$_3$O$_4$.

concentrations over 0.6Pt/meso-Co$_3$O$_4$, 1.0Pt/meso-Co$_3$O$_4$ and 0.6Pt/bulk-Co$_3$O$_4$ catalysts are 42.9%, 37.5% and 35.9%. It is attributed to the dispersive Pt particles on the Co$_3$O$_4$ and the formation of Pt–O–Co bond. Therefore, it is concluded that

Table 2 Surface states of Pt species derived from XPS analyses

Catalyst	Pt^0 (%)	Pt^{2+} (%)	Pt^{4+} (%)
0.6Pt/meso-Co_3O_4	57.1	29.7	13.2
1.0Pt/meso-Co_3O_4	62.5	27.4	10.1
0.6Pt/bulk-Co_3O_4	64.2	19.4	16.5

there is an electron transfer from Pt to Co^{3+} after the loading of Pt particles. It is consistent with the result of Raman characterization. 0.6Pt/meso-Co_3O_4 possesses higher concentrations of $Pt^{\delta+}$ than 1.0Pt/meso-Co_3O_4, and thus increases the density of active oxygen species and Co^{2+} species of 0.6Pt/meso-Co_3O_4. Meanwhile, 0.6Pt/meso-Co_3O_4 shows higher concentrations of $Pt^{\delta+}$ in the meso-Co_3O_4 surface than 0.6Pt/bulk-Co_3O_4. It should be due to the order mesoporous structure of meso-Co_3O_4. Co 2p shows four peaks at BE = 779.5, 780.7, 794.5 and 796.9 eV, which corresponds to Co^{3+} $2p_{3/2}$, Co^{2+} $2p_{3/2}$, Co^{3+} $2p_{1/2}$ and Co^{2+} $2p_{1/2}$ (ref. 11) in Fig. 6B. Table 3 lists the surface Co^{3+}/Co^{2+} molar ratios of the catalysts. The existence of surface oxygen vacancies is further confirmed by the XPS. The surface Co^{3+}/Co^{2+} molar ratios of bulk-Co_3O_4 are higher than meso-Co_3O_4. Compared to the meso-Co_3O_4 and bulk-Co_3O_4, the Co^{3+}/Co^{2+} molar ratios of xPt/meso-Co_3O_4 and 0.6Pt/bulk-Co_3O_4 catalysts decrease, indicating that the surface Co^{2+} concentration increases after Pt loading. xPt/meso-Co_3O_4 possess a higher oxygen vacancy concentration than meso-Co_3O_4. It should be due to the electron transfer from Pt to Co^{3+} through the reaction of $Pt^0 + Co^{3+} \rightarrow Pt^{\delta+} + Co^{2+}$. 0.6Pt/meso-$Co_3O_4$ gives the minimum value of the surface Co^{3+}/Co^{2+} molar ratio and the most surface oxygen vacancy. From Fig. 6C, O 1s exhibits two peaks at 529.6 and 531.0 eV. The former can be assigned to the surface lattice oxygen (O_{latt}), and the latter corresponds to surface adsorbed oxygen (O_{ads}).[24] It is widely recognized that the O_{ads} species play an important role in the deep oxidation of the organics.[25] Combined with the results from Table 3, the O_{ads}/O_{latt} molar ratio (0.98) of bulk-Co_3O_4 is lower than those of meso-Co_3O_4 (1.20) and of xPt/meso-Co_3O_4 (1.25–1.44), indicating that meso-Co_3O_4 possess more adsorbed oxygen species. The highest O_{ads}/O_{latt} molar ratio of 0.6Pt/meso-Co_3O_4 is 1.44, and thus

0.6Pt/meso-Co_3O_4 has the most surface absorbed oxygen species.

3.3. The results of O_2-TPD

To further study the effect of activated oxygen species for acetylene oxidation, O_2-TPD experiments are carried out. The result is shown in Fig. 7. The desorption peak that are less than 450 °C can be ascribed to surface active oxygen, such as O_2^- and O^-, and the desorption temperature of bulk phase lattice oxygen are higher than 700 °C.[11] Compared with meso-Co_3O_4, xPt/meso-Co_3O_4 presents higher intensities of desorption peaks below 450 °C. This phenomenon indicates that xPt/meso-Co_3O_4 surface contains more abundant surface active oxygen species than meso-Co_3O_4. It is in according with the result of XPS. For 0.3Pt/meso-Co_3O_4, the desorption peak is centered at 443 °C. For 1.0Pt/meso-Co_3O_4, the desorption peak shifts to lower temperature range, starting at 300 °C and is centered at 425 °C. Among xPt/meso-Co_3O_4, 0.6Pt/meso-Co_3O_4 exhibits the lowest beginning oxygen desorption temperature and highest intensities of desorption peak. The desorption temperature and intensity of surface-active oxygen species are connected to the catalytic ability for oxidation reaction. Lower beginning oxygen desorption temperatures and larger intensities of desorption peaks lead to better catalytic ability.[11] It indicates that the adding of Pt is beneficial to increasing the surface activity oxygen species of xPt/meso-Co_3O_4, which can enhance the catalytic performance of acetylene oxidation.

3.4. The results of H_2-TPR

Low-temperature reducibility is an important factor in oxidation reactions. H_2-TPR experiments are carried to investigate the reducibility of the samples. The results are shown in Fig. 8. For the bulk-Co_3O_4, there are two reduction peaks at 364 °C and 473 °C. For the meso-Co_3O_4, there are two reduction peaks at 308 °C and 450 °C. The former is due to the reduction of Co_3O_4 to CoO, whereas the latter is attributed to the reduction of CoO
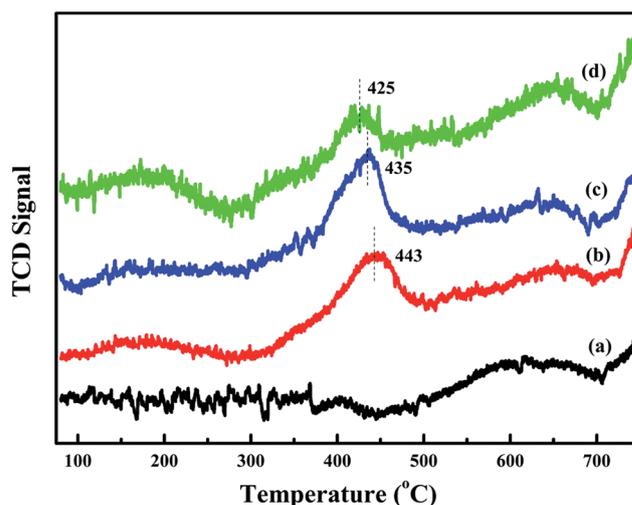
Table 3 Surface compositions and apparent activation energies of the bulk-Co_3O_4, 0.6Pt/bulk-Co_3O_4, meso-Co_3O_4 and xPt/meso-Co_3O_4 samples for acetylene oxidation

Catalyst	Co^{3+}/Co^{2+} molar ratio	O_{ads}/O_{latt} molar ratio	H_2 consumption (mmol g^{-1})	E_a (kJ mol^{-1})
Meso-Co_3O_4	0.69	1.20	16.1	77
0.3Pt/meso-Co_3O_4	0.65	1.31	15.4	50
0.6Pt/meso-Co_3O_4	0.60	1.44	14.6	46
1.0Pt/meso-Co_3O_4	0.66	1.25	15.6	48
Bulk-Co_3O_4	0.83	0.98	16.9	99
0.6Pt/bulk-Co_3O_4	0.73	1.07	16.0	68

Fig. 7 O_2-TPD profiles of (a) meso-Co_3O_4, (b) 0.3Pt/meso-Co_3O_4, (c) 0.6Pt/meso-Co_3O_4 and (d) 1.0Pt/meso-Co_3O_4.
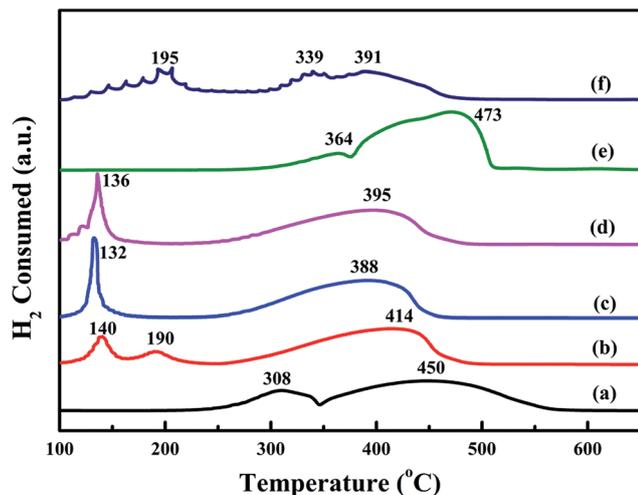
Fig. 8 H$_2$-TPR profiles of (a) meso-Co$_3$O$_4$, (b) 0.3Pt/meso-Co$_3$O$_4$, (c) 0.6Pt/meso-Co$_3$O$_4$, (d) 1.0Pt/meso-Co$_3$O$_4$, (e) bulk-Co$_3$O$_4$ and (f) 0.6Pt/bulk-Co$_3$O$_4$.

to Co^0. Comparing the reduction profile of bulk-Co$_3$O$_4$, meso-Co$_3$O$_4$ is more reducible at lower temperatures. Therefore, meso-Co$_3$O$_4$ with high surface area displays a more amount of reducible sites. After the adding of Pt, there is a new reduction peak at 140 °C for 0.3Pt/meso-Co$_3$O$_4$. It should be due to the reduction of Pt$^{\delta+}$. Meanwhile, the reduction peaks of Co$_3$O$_4$ to CoO and CoO to Co^0 shift to lower temperatures. For 0.6Pt/meso-Co$_3$O$_4$ and 1.0Pt/meso-Co$_3$O$_4$, the reduction peaks of Pt$^{\delta+}$ to Pt^0 and Co^{3+} to Co^{2+} are overlapped. 0.6Pt/meso-Co$_3$O$_4$ presents the lowest reduction peak at 132 °C. It indicates that the adding of Pt gives rise to the improvement in low-temperature reducibility of xPt/meso-Co$_3$O$_4$, which can enhance the catalytic performance of acetylene oxidation. Meanwhile, 0.6Pt/meso-Co$_3$O$_4$ displays the highest ability of low-temperature reducibility. By quantitatively analyzing the reduction peaks in H$_2$-TPR profiles, the H$_2$ consumption of the samples are shown in Table 3. The H$_2$ consumption of meso-Co$_3$O$_4$, 0.3Pt/meso-Co$_3$O$_4$, 0.6Pt/meso-Co$_3$O$_4$, 1.0Pt/meso-Co$_3$O$_4$, bulk-Co$_3$O$_4$ and 0.6Pt/bulk-Co$_3$O$_4$ is 16.1, 15.4, 14.6, 15.6, 16.9 and 16.0 mmol g^{-1}, respectively. Due to the presence of the partially overlapping reduction of Co^{3+}, Co^{2+} and Pt$^{\delta+}$ ions, it is hard to convert the H$_2$ consumption to the Co^{3+}/Co^{2+} ratios and the content of the Pt$^{\delta+}$. However, it can conclude that there are more amounts of oxygen vacancies in xPt/Co$_3$O$_4$ than in pure Co$_3$O$_4$. It is in good agreement with their Raman and XPS results.

3.5. Catalytic performance

In order to eliminate influence of diffusion, the kinetics research of acetylene oxidation is first carried out. Fig. 9a shows the reaction results for meso-Co$_3$O$_4$ catalyst at various space velocities. In the absence of mass-transfer limitations, acetylene conversion is excepted to increase by n-fold as the space velocity decrease by n-fold. Acetylene conversion ratios (Fig. 9b) suggest that meso-Co$_3$O$_4$ should decrease the influence of diffusion
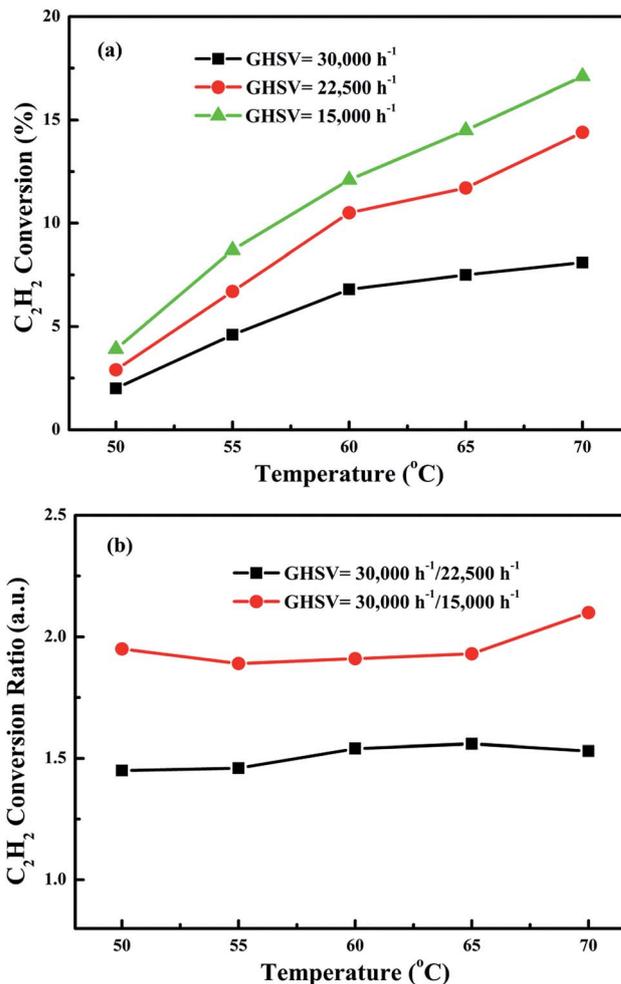

Fig. 9 (a) Acetylene conversion as a function of reaction temperature over meso-Co$_3$O$_4$ at space velocities of 15 000 h^{-1}, 22 500 h^{-1} and 30 000 h^{-1} and (b) acetylene conversion ratios for 15 000 h^{-1}, 22 500 h^{-1} and 30 000 h^{-1} as a function of reaction temperature, using date from (a).

under 30 000 h^{-1} space velocity. Fig. 10 shows the catalytic performances of the catalysts for the oxidation of acetylene. It is evident that the most effective catalyst for acetylene oxidation is 0.6Pt/meso-Co$_3$O$_4$, while the worst active catalyst is bulk-Co$_3$O$_4$. The order of the catalytic activity is 0.6Pt/meso-Co$_3$O$_4$ > 1.0Pt/meso-Co$_3$O$_4$ > 0.3Pt/meso-Co$_3$O$_4$ > meso-Co$_3$O$_4$ > bulk-Co$_3$O$_4$, in good agreement with the reducibility sequences of these catalysts. The bulk-Co$_3$O$_4$ catalyst displays the worst catalytic activity, and the complete conversion temperature of acetylene is at 220 °C. The meso-Co$_3$O$_4$ catalyst shows better oxidation activity, completely converting acetylene at 160 °C. Among xPt/meso-Co$_3$O$_4$ catalysts, 0.6Pt/meso-Co$_3$O$_4$ catalyst exhibits the best catalytic performance, which can completely oxidize acetylene at 120 °C. Fig. 11 shows the Arrhenius plots for acetylene oxidation over the Co$_3$O$_4$ and xPt/Co$_3$O$_4$, and the calculated apparent activation energies (E_a) are summarized in Table 3. It is shown that the E_a value for acetylene oxidation decreased in the sequence of bulk-Co$_3$O$_4$ > meso-Co$_3$O$_4$ > 0.6Pt/bulk-Co$_3$O$_4$ > 0.3Pt/meso-Co$_3$O$_4$ > 1.0Pt/meso-Co$_3$O$_4$ > 0.6Pt/meso-Co$_3$O$_4$. The
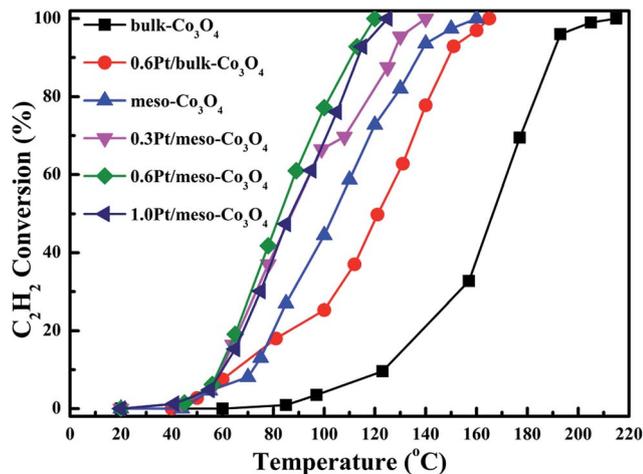
Fig. 10 Catalytic performance as a function of reaction temperature over bulk-Co_3O_4, 0.6Pt/bulk-Co_3O_4, meso-Co_3O_4, 0.3Pt/mso-Co_3O_4, 0.6Pt/meso-Co_3O_4 and 1.0Pt/meso-Co_3O_4 catalysts for the oxidation of C_2H_2 under the conditions: $[C_2H_2]$ = 50 ppm, $[O_2]$ = 13 vol%, N_2 balance and GHSV = 30 000 h^{-1}.
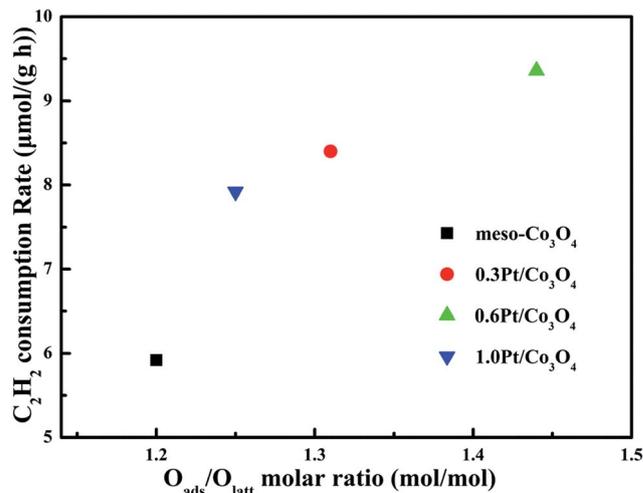
Fig. 12 Acetylene consumption rates at 60 °C as a function of O_{ads}/O_{latt} molar ration of meso-Co_3O_4, 0.3Pt/meso-Co_3O_4, 0.6Pt/meso-Co_3O_4 and 1.0Pt/meso-Co_3O_4. Reaction gas composition: $[C_2H_2]$ = 50 ppm, $[O_2]$ = 13 vol%, N_2 balance and GHSV = 30 000 h^{-1}.
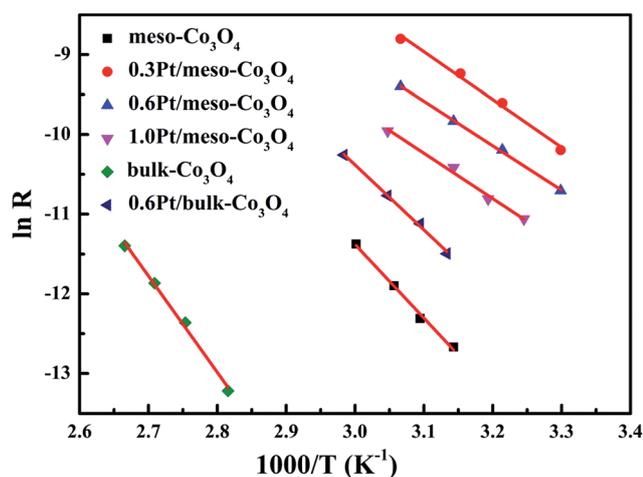
Fig. 11 Arrhenius plots in acetylene oxidation of meso-Co_3O_4, 0.3Pt/meso-Co_3O_4, 0.6Pt/meso-Co_3O_4, 1.0Pt/meso-Co_3O_4, bulk-Co_3O_4 and 0.6Pt/bulk-Co_3O_4. Reaction gas composition: $[C_2H_2]$ = 50 ppm, $[O_2]$ = 13 vol%, N_2 balance and GHSV = 30 000 h^{-1}.

Fig. 13 Durability test on 0.6Pt/meso-Co_3O_4 catalyst. Reaction gas composition: $[C_2H_2]$ = 50 ppm, $[O_2]$ = 13 vol%, N_2 balance and GHSV = 30 000 h^{-1}.

apparent activation energy of 0.6Pt/meso-Co_3O_4 is the lowest. The oxidation of acetylene might be more easily over the mesoporous Co_3O_4 supported Pt catalysts. For the xPt/meso-Co_3O_4 samples, Pt particles are dispersed on the surface of meso-Co_3O_4, and more oxygen vacancies are present in xPt/meso-Co_3O_4. O_{ads} is a beneficial role with respect to catalytic oxidation of acetylene. To further study the effect of O_{ads} in acetylene oxidation. Then, a test is carried out at low conversions under a kinetically controlled regime at 60 °C. As shown in Fig. 12, the acetylene consumption rate increases with the rising of O_{ads}/O_{latt} molar ratio. That is to say, a higher O_{ads} concentration is beneficial for the enhancement in catalytic oxidation of acetylene.

In order to examine the chemical and mechanical stability of the catalysts, the on-steam reaction experiments were carried
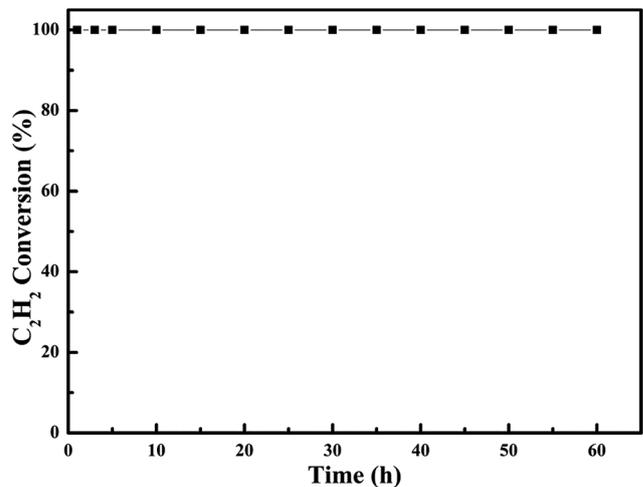
out over the most effective 0.6Pt/meso-Co_3O_4 at 120 °C for acetylene oxidation, as shown in Fig. 13. There is no significant loss in catalytic activity. It indicates that 0.6Pt/meso-Co_3O_4 catalyst is chemical stability for acetylene oxidation. SEM images of the recovered catalyst are shown in Fig. 14. The morphology of the catalyst did not show significant change. Therefore, 0.6Pt/meso-Co_3O_4 may be a chemical and mechanical durable catalyst for acetylene oxidation under the adopted conditions.

It is generally known that the porous network of catalysts can provide more contact sites and promote the diffusion of reactant and product molecules. The mesoporous structure is beneficial to enhancing the catalytic oxidation of acetylene. The big surface area of meso-Co_3O_4 (122.0 m^2 g^{-1}) is highly conductive to acetylene oxidation. xPt/meso-Co_3O_4 also possess
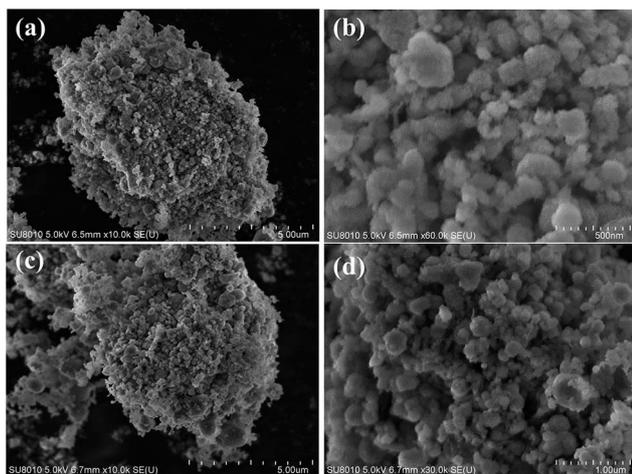
Fig. 14 SEM images of (a and b) 0.6Pt/meso-Co$_3$O$_4$ catalyst and (c and d) the used 0.6Pt/meso-Co$_3$O$_4$.

the high surface area (111.0–111.5 m^2 g^{-1}). After the loading of Pt, xPt/meso-Co$_3$O$_4$ catalysts exhibit higher conversion at low temperature than meso-Co$_3$O$_4$ catalyst. The reaction mechanism of C$_2$H$_4$ oxidation over the Co$_3$O$_4$ has been reported.[26] It was reported that the oxidation of hydrocarbons on transition metal oxides follows a Mars-Van Krevelen mechanism.[27] The surface oxygen species will participate in hydrocarbons oxidation process and recovery by the gas-phase oxygen molecules. Thus, the reaction mechanism of acetylene oxidation over the catalysts may be related to surface oxygen species. Acetylene molecule can be absorbed on the surface of xPt/meso-Co$_3$O$_4$ to form an adsorbed intermediate. The adsorbed acetylene species are further oxidized to CO$_2$ and H$_2$O under the effect of surface active oxygen. From the results of XPS and O$_2$-TPD, xPt/meso-Co$_3$O$_4$ display more surface absorbed oxygen species than meso-Co$_3$O$_4$. The existence of lattice defect is beneficial for the formation of the oxygen vacancies. The oxygen vacancies can be favorable for the adsorption of oxygen and hence enhancing the catalytic oxidation of acetylene. xPt/meso-Co$_3$O$_4$ exhibit more lattice defect than meso-Co$_3$O$_4$, which can be demonstrated from the result of Raman, XPS and H$_2$-TPR. It has been reported that better catalytic activity is related to low-temperature reducibility. Better reducibility means that oxygen species are easily activated. From the result of H$_2$-TPR, xPt/meso-Co$_3$O$_4$ show better low-temperature reducibility than meso-Co$_3$O$_4$. Among all xPt/meso-Co$_3$O$_4$ catalysts, 0.6Pt/meso-Co$_3$O$_4$ catalyst exhibits the best catalytic performance, which can completely oxidize acetylene at 120 °C. 0.6Pt/meso-Co$_3$O$_4$ shows orderedly mesoporous structure, sufficient oxygen vacancies, more adsorbed oxygen species and better low-temperature reducibility. Therefore, the highest catalytic performance of 0.6Pt/meso-Co$_3$O$_4$ for the oxidation of acetylene was obtained.

4. Conclusions

The meso-Co$_3$O$_4$ with high surface area are synthesized by using the KIT-6 hard template, and xPt/meso-Co$_3$O$_4$ catalysts are prepared by the means of NaBH$_4$ reduction. The activity for acetylene oxidation over different catalysts decreases in the following order: 0.6Pt/meso-Co$_3$O$_4$ > 1.0Pt/meso-Co$_3$O$_4$ > 0.3Pt/meso-Co$_3$O$_4$ > meso-Co$_3$O$_4$ > bulk-Co$_3$O$_4$. 0.6Pt/meso-Co$_3$O$_4$ exhibits the highest catalytic activity of acetylene oxidation at 120 °C and good stability for at least 60 h. The excellent catalytic performance of 0.6Pt/meso-Co$_3$O$_4$ can be associated with its orderedly mesoporous structure, plenty of adsorption oxygen species and better low-temperature reducibility.

Acknowledgements

References

1 K. Wang, L. Du and M. F. Ge, J. Environ. Sci., 2009, 21, 137–141.

2 R. Volkamer, P. J. Ziemann and M. J. Molina, Atmos. Chem. Phys., 2009, 9, 1907–1928.

3 W. P. L. Carter, Air Waste, 1994, 44, 881–899.

4 Y. Yu, T. Takei, H. Ohashi, H. He, X. Zhang and M. Haruta, J. Catal., 2009, 267, 121–128.

5 C. Y. Ma, Z. Mu, J. J. Li, Y. G. Jin, J. Cheng, G. Q. Lu, Z. P. Hao and S. Z. Qiao, J. Am. Chem. Soc., 2010, 132, 2608–2613.

6 C. Ma, D. Wang, W. Xue, B. Dou, H. Wang and Z. Hao, Environ. Sci. Technol., 2011, 45, 3628–3634.

7 Z. Wang, W. Wang, L. Zhang and D. Jiang, Catal. Sci. Technol., 2016, 6, 3845–3853.

8 Y. Xia, H. Dai, H. Jiang and L. Zhang, Catal. Commun., 2010, 11, 1171–1175.

9 J. Yang and T. Sasaki, Cryst. Growth Des., 2010, 10, 1233–1236.

10 L. Hu, Q. Peng and Y. Li, J. Am. Chem. Soc., 2008, 130, 16136–16137.

11 B. Bai, H. Arandiyan and J. Li, Appl. Catal., B, 2013, 142–143, 677–683.

12 C. Zhang, F. Liu, Y. Zhai, H. Ariga, N. Yi, Y. Liu, K. Asakura, M. Flytzani-Stephanopoulos and H. He, Angew. Chem., Int. Ed., 2012, 51, 9628–9632.

13 C. Zhang and H. He, Catal. Today, 2007, 126, 345–350.

14 X. Tang, J. Chen, X. Huang, Y. Xu and W. Shen, Appl. Catal., B, 2008, 81, 115–121.

15 F. Kleitz, S. H. Choi and R. Ryoo, Chem. Commun., 2003, 2136–2137.

16 A. Rumplecker, F. Kleitz, E. L. Salabas and F. Schüth, Chem. Mater., 2007, 19, 485–496.

17 M. Casas-Cabanas, G. Binotto, D. Larcher, A. Lecup, V. Giordani and J.-M. Tarascon, Chem. Mater., 2009, 21, 1939–1947.

18 Q. Liu, L. C. Wang, M. Chen, Y. Cao, H. Y. He and K. N. Fan, J. Catal., 2009, 263, 104–113.

19 K. R. Zhu, M. S. Zhang, Q. Chen and Z. Yin, *Phys. Lett. A*, 2005, **340**, 220–227.

20 Y. Liu, H. Dai, J. Deng, S. Xie, H. Yang, W. Tan, W. Han, Y. Jiang and G. Guo, *J. Catal.*, 2014, **309**, 408–418.

21 M. M. Schubert, S. Hackenberg, A. C. van Veen, M. Muhler, V. Plzak and R. J. Behm, *J. Catal.*, 2001, **197**, 113–122.

22 Y. Li, Y. Du, Y. Wei, Z. Zhao, B. Jin, X. Zhang and J. Liu, *Catal. Sci. Technol.*, 2017, **7**, 968–981.

23 W. Tang, Z. Hu, M. Wang, G. D. Stucky, H. Metiu and E. W. Mcfarland, *J. Catal.*, 2010, **273**, 125–137.

24 B. Bai and J. Li, *ACS Catal.*, 2014, **4**, 2753–2762.

25 S. Rousseau, S. Loridant, P. Delichere, A. Boreave, J. P. Deloume and P. Vernoux, *Appl. Catal., B*, 2009, **88**, 438–447.

26 H. F. Feng, D. Wang, X. H. Liu, Y. L. Guo, G. Z. Lu and P. J. Hu, *ACS Catal.*, 2016, **6**, 5393–5398.

27 S. Scirè and L. F. Liotta, *Appl. Catal., B*, 2012, **125**, 222–246.